The Atmospheric Response to an Unusual Early-Year Martian Dust Storm

Cong Sun[1], Chengyun Yang[1,2*], Xin Fang[1,2] and Tao Li[1,2*]

[1] CAS Key Laboratory of Geospace Environment, School of Earth and Space Sciences, University of Science and Technology of China, Hefei, Anhui, China

[2] CAS Center for Excellence in Comparative Planetology, University of Science and Technology of China, Hefei, Anhui, China

Corresponding author: Chengyun. Yang, cyyang@ustc.edu.cn, Tao. Li, litao@ustc.edu.cn

Abstract

During the northern spring (approximately Ls≈33°) in Martian Year 35, Mars experienced an unusual dust storm characterized by significantly increased dust in the northern troposphere. As observed by the Mars Climate Sounder (MCS), temperature significantly increases in the mid-latitude troposphere of both hemispheres and decreases in the northern mesosphere during the event. The temperature response simulated by the Martian General Circulation Model (GCM) agrees with the MCS observations. The radiative heating from dust is responsible for the increased temperature in the northern troposphere. In contrast, the dynamic heating/cooling contributes to the temperature variations in the southern troposphere and northern mesosphere. The increased dissipation of planetary waves enhances the residual meridional circulation and causes the temperature warming in the Southern Hemisphere. In addition, the enhanced meridional circulation related to this event leads to ~36% increase in water vapor transport from the Northern to the Southern Hemisphere as compared to the net interhemispheric transport over an entire Martian Year.

Key Points

1. Global atmospheric responses are observed during an early-year dust event in the northern spring.
2. Direct solar heating warms the dust-lifting zone, with dynamic processes influencing temperature responses in two other remote regions.
3. The anomalous residual circulation induced by atmospheric waves leads to increased water transport into the Southern Hemisphere.

Plain Language Summary

Using orbital observation and general circulation model data, this study provides a detailed account of an unusual regional dust storm in the Northern Hemisphere of Mars during its cold and clear season. This dust storm triggered atmospheric temperature responses in the Northern Hemisphere, where dust storms occurred, and in the Southern Hemisphere middle latitude regions. Direct solar radiative absorption by dust particles predominantly drives the heating in the mid-latitudes of the northern troposphere. The temperature variations in the northern upper atmosphere and the southern hemisphere are due to the thermal contributions of dynamic processes, specifically the effects of gravity waves and planetary waves. As unusual wave activities intensified the trans-equatorial meridional circulation amidst dust events, there was a significant increase in water transport from the Northern Hemisphere to the Southern Hemisphere. This increase contributes to approximately 36% of north to south water transport during the Martian Year 35. This shift could be attributed to the enhancement of the meridional circulation induced by dust storms.

1. Introduction

The activities of Martian dust significantly affect the spatial and temporal variations of the Martian atmosphere,. (Kahre et al., 2017; Kass et al., 2016). Depending on the spatial scale, Martian dust activity includes global dust storms that can cover the entire planet (Zurek and Martin, 1993), regional dust storms affecting specific areas (typically covering 1.6×10^6 km2), localized dust storms, and phenomena such as dust devils (Cantor, 2007; Cantor et al., 2001; Wang & Richardson, 2015; Wu, et al., 2022). As suggested by previous studies, the dust storms can induce the temperature and density perturbations from the lower to upper atmosphere (Fang et al., 2020; Girazian et al., 2020), the variation of ice clouds (Kleinböhl et al., 2009; Liuzzi et al., 2020; Montmessin et al., 2002), and the propagation of water vapor (Fang et al., 2020; Fedorova et al., 2018; Heavens et al., 2018; Huang et al., 2022; Li et al., 2020; Wu et al., 2020; Wu et al., 2022). Dust storms can not only affect the local atmosphere (Haberle et al., 2017) but also influence regions distant from the dust-active region by atmospheric dynamics (Guzewich et al., 2016; Heavens et al., 2011; Streeter et al., 2021).

Most dust events occurred during the northern autumn and winter due to the substantially increased insolation near the perihelion, coinciding with the northern winter solstice. (Kass et al., 2016; Li et al., 2020). During the northern spring (Ls 0 to 120°), as Mars approaches its aphelion, it experiences relatively colder temperatures and lower concentrations of free aerosol dust particles in the atmosphere (Montabone et al., 2015, 2020). Thus, dust activity is usually weak during this period. Recently, an unusual regional dust storm (so-called Early Event or E Event hereafter) was observed from Ls≈ $35^{\circ}$to 50°in Martian Year 35 (MY35) according to images from the Mars Reconnaissance Orbiter (MRO) Mars Color Imager (MARCI) (Kass et al., 2022.; Montabone et al., 2020). The regional dust storm initialized near the northwest of Olympus Mons and quickly expanded to a regional dust storm in 4 solar days (sols) (Kass et al., 2022). The atmosphere is cold and lacks solar radiation during this period as compared with that during the second half of the year (Clancy et al., 2021; Guha et al., 2021a; Määttänen & Montmessin, 2021; Mateshvili et al., 2007).

This unusual E event provides a distinct case for understanding the dynamic and thermal coupling mechanisms under the atmospheric backgrounds in this cold Martian season. The primary objective of this article is to investigate the response of the Martian atmosphere to an unusual early dust event occurring in the northern spring. The satellite observations, general circulation mode used in this study, and the analysis method are introduced in Section 2. The temperature responses to the E Event and the underlying mechanism are investigated in Section 3. Section 4 discussed the dynamic responses and the potential impact on interhemispheric water transport. A summary is provided in Section 5.

2. Data and Method

2.1 Observations and simulations

The Mars Climate Sounder (MCS) onboard the MRO, launched in August 2005, has measured the Martian atmosphere from the near-surface to ~80 km in a sun-synchronous (~0300 LT and ~1500 LT) polar orbit since September 2006, covering all of the dust events from MY27-MY37 (Creasey et al., 2006; Lee et al., 2009; McCleese et al., 2007). The MCS repetitively measures the Martian atmosphere through nadir/off-nadir and limb sounding (Kleinböhl et al., 2009). Profiles of temperature, dust, and water ice with ~5 km vertical resolution are obtained by tuning the horizontal resolution to achieve an enhanced vertical resolution (McCleese et al., 2007). The dust and water ice quantities are provided in units of extinction per unit height due to dust at 463 cm^{-1} and water ice at 843 cm^{-1} (McCleese et al., 2007).

The Martian general circulation model (GCM) developed at the Dynamic Meteorology Laboratory (LMD) (Forget et al., 1999) model consists of a dynamical core that uses a finite difference method to solve basic hydrodynamic equations and a physical core; this model considers a series of comprehensive processes, such as radiative transfer(Forget, 1998; Wolff et al., 2006, 2009), the dust cycle(J.-B. Madeleine et al., 2011), the water cycle(J. -B. Madeleine, Forget, Millour, et al., 2012;

J. -B. Madeleine et al., 2014; Montmessin et al., 2004; Navarro et al., 2014), and energy and material transfer in the PBL region(Colaïtis et al., 2013). This study conducts simulations with a resolution of 5.625×3.75◦ in the horizontal direction and 29 p-levels in the vertical direction from the ground to 100 km. To correspond with the dust scenario during the E Event in MY35, the MY35 reconstructed dust map is used as the initial model file (a detailed reference of the dust map can be found in (Montabone et al., 2015, 2020).

2.2 Methods

The satellite observations are binned into $30^{\circ} \times 10^{\circ}$ longitude-latitude bins at every pressure level, as discussed in Wu et al. (2015, 2017, 2020). Since the longitudinal coverages of ~ 3 a.m. and ~ 3 p.m. are the local times with the most samples due to the dominant in-track observation strategy (Kleinböhl et al., 2013), the daily means are calculated by averaging the mean values during the day and night. The zonal mean values are calculated only for longitude bins exceeding nine (Wu et al., 2020). The dust opacity depth in the MCS observations is weighted by the density ($(d_z\tau)/\rho$), which is proportional to the mass mixing ratio (Heavens et al., 2011; Wu et al., 2021). $d_z\tau$ refers to the opacity depth, while the atmospheric density ρ is derived from the pressure and temperature in MCS observations according to the ideal gas assumption. The climatology in the MCS observation is determined as the mean value in each Ls from MY27 to MY37, while the data in the MY35 are excluded. The climatological case of the LMD is simulated from the prescribed climatological dust scenario as described in (Montabone et al., 2015, 2020).

To investigate the radiative and dynamic responses in the Martian atmosphere during the E Event period, the transformed Eulerian mean (TEM) zonal momentum and thermodynamic budget analysis are used in this study, as discussed in (Andrews et al., 1987; Keeble et al., 2014; Orr, Bracegirdle, Hosking, Feng, et al., 2012; Orr, Bracegirdle, Hosking, Jung, et al., 2012), as follows:

$$[u]_t + \zeta_a[v]^\dagger + [w]^\dagger[u]_z - [X] = \frac{1}{\rho_0\, a\cos\phi}\nabla\cdot\mathbf{F} \quad (1)$$

$$[\theta]_t + \frac{1}{a}[v]^\dagger[\theta]_\phi + [w]^\dagger[\theta]_z - [Q_{\mathrm{dia}}] = -\frac{1}{\rho_0}\left\{\rho_0\left(\frac{[v^*\theta^*][\theta_\phi]}{a[\theta]_z} + [w^*\theta^*]\right)\right\}_z \quad (2)$$

where u, v and w are the zonal, meridional and vertical components of the wind field, respectively; a is the Martian radius; f is the Coriolis parameter; ϕ is latitude; z is height; ρ_0 is air density, which can be calculated with the relationship of the density scale height H (10 km) as $\exp(-\mathrm{z/H})$; θ is the potential temperature;$\zeta_a = (a\cos\phi)^{-1}([u]\cos\phi)_\phi - f$; $[v]^\dagger$ and $[w]^\dagger$ denote the TEM residual meridional and vertical winds, which are defined as $[v]^\dagger = [v] - \rho_0^{-1}(\rho_0[v^*\theta^*]/[\theta]_z)_z$ and $[w]^\dagger = [w] + (a\cos\phi)^{-1}(\cos\phi[v^*\theta^*]/[\theta]_z)_\phi$. The equation's square brackets indicate the zonal mean; the asterisks are used for the zonal anomalies (total waves that deviate from the zonal mean in all frequencies); the subscripts indicate the partial derivative for certain coordinates. The term $[X]$ represents unresolved forcing, such as unresolved gravity waves (GWs), smaller-scale turbulent diffusion, and friction. Limited by the size of the model grid, the effects of GWs are parameterized (Gilli et al., 2020; Liu et al., 2023; Lott & Millet, 2010) in the LMD-GCM model.

The divergence of the Eliassen–Palm (EP) flux, which is associated with resolved planetary wave (PW) activities, can be expressed as (Andrews et al., 1987):

$$F_y = \rho_0 a\cos\phi\left(-[u^*v^*] + \frac{[u]_z[v^*\theta^*]}{[\theta_z]}\right), \quad (3)$$

$$F_z = \rho_0 a\cos\phi\left(\frac{-\zeta_a[v^*\theta^*]}{[\theta_z]} - [u^*w^*]\right), \quad (4)$$

$$\nabla\cdot\mathbf{F} = \frac{1}{a\cos\phi}\frac{\partial(F_y\cos\phi)}{\partial\phi} + \frac{\partial F_z}{\partial z}. \quad (5)$$

where F_y and F_z represent the zonal and vertical components of the EP flux, respectively; and the $\nabla\cdot\mathbf{F}$ term indicates the EP flux divergence (EPD). The EP flux represents the transport of resolved wave energy and momentum in the atmosphere (Andrews, 1987; Andrews et al., 1987; Becker, 2012).

The heating rate in the atmosphere can be divided into two parts: the total dynamic heating rate (temperature tendency $[\theta]_t$ due to dynamic processes) and the radiative heating (including shortwave and longwave radiative heating). The radiative heating terms can be directly obtained from the model outputs. The total dynamic heating rates can be computed by rearranging the TEM thermodynamic equation et al., 2012) as follows:

$$[Q_{\mathrm{dyn}}]^{\theta} = -\frac{1}{\rho_0}\left\{\rho_0\left(\frac{[v^*\theta^*][\theta_\phi]}{a[\theta]_z} + [w^*\theta^*]\right)\right\}_z - \frac{1}{a}[v]^{\dagger}[\theta]_\phi - [w]^{\dagger}[\theta]_z \quad (6)$$

Where the term $(-a^{-1}[v]^{\dagger}[\theta]_\phi - [w]^{\dagger}[\theta]_z)$ refers to the advective heating rate $[Q_{\mathrm{dyn}}]^{\theta}$, while the first term on the right-hand side (RHS) represents the dynamical term of quasi-geostrophic motion (e.g., eddy-heat flux term). In the TEM framework, $[Q_{\mathrm{dyn}}]^{\theta}$ is converted from the potential temperature–time tendency to the temperature tendency as $[Q_{\mathrm{dyn}}]^{\theta} = [Q_{\mathrm{dyn}}]^{\theta}(p/p_0)^{R/C_P}$, where R is the ideal gas constant and C_p is the specific heat capacity.

The meridional flux of the mass transport across the equator can be calculated as follows:

$$\int_{hs}^{he} 2\pi a\, cos(\phi) \times \delta_z \times [v]^{\dagger} \times \rho \times \chi_{h2o} \mathrm{dz} \quad (7)$$

where hs and hs indicate the height ranges (start height and end height, respectively); δ_z is the layer height in m; and χ_{h2o} is the volume mixing ratio from the LMD model. The definite integral of the mass flux quantitatively calculates the amount of trans-equatorial moisture over a specific period.

3 Results

Figure 1a shows the variations of the zonal mean total column dust opacity depth (CDOD) (Montabone et al., 2020) and temperature with solar longitude (Ls) during the E event from MCS observations. As mentioned by Kass et al. (2022) and

Montabone et al. (2020), the CDOD enhanced (with a maximum of 0.25) from the equator to nearly 60°N in the early spring of MY35 (from Ls≈34° to Ls≈55°). Meanwhile, an enhanced CDOD (~0.12) is also observed in the Southern Hemisphere. The anomalous dust mixing ratio is positive in the northern troposphere, with a maximum of approximately $0.03 m^2/kg$ in the middle latitudes. The density-scaled CDOD anomalies are also positive in the southern troposphere, with a maximum of approximately $0.02 m^2/kg$ **(Figure 1b)**. In the LMD simulation (**Figure 1c**), there are also positive dust mass mixing ratio anomalies located at the northern middle latitudes, with a maximum of $\sim 2 \times 10^{-6} kg/kg$ near the surface.

The MCS observations recorded significant positive temperature anomalies near Ls$\approx 35^{\circ}$, with a maximum of 13 K in the northern mid-latitudes (30°-60°N) from 20 to 40 km **(Figure 1d**), associated with the anomalous cooling in the northern mesosphere (around 60 km). Positive temperature anomalies are also observed in the southern troposphere, with a maximum of approximately 6 K at 40°S, 25 km. In the tropical region, the positive temperature anomalies extend from the near-surface to 60 km. The temperature anomalies in the LMD simulation basically agree with those in the MCS observations, with increased temperatures in the mid-latitude troposphere in both hemispheres associated with decreased temperatures in the northern mesosphere. In the southern hemisphere, the anomalous cooling (approximately -1.3 K) is weaker in the LMD simulation. As the simulated dust amount was lower in the LMD than in the MCS observations, it could lead to inconsistency of the temperature response to the early dust storms. Given the overall agreement in the temperature responses with the MCS observations, LMD simulations are used to investigate the underlying mechanisms of the atmospheric response to rare E events.

As both dynamic/adiabatic and radiative/diabatic processes can influence the atmospheric temperature, a decomposition of the heating rate was adopted to investigate the mechanisms in which Northern Hemisphere dust storms could affect the global temperature. As shown in **Figure 2a**, the middle latitudes of the northern troposphere (from 30°N to 60°N, extending from near the surface up to 40 km) which is classified as Region 1 (R1 hereafter) became warmer than normal during the E event. The temperature anomalies are negative in the northern lower mesosphere ($30^{\circ}-60^{\circ}$N, 45 to 70 km, Region 2; R2). The area ranging from $30^{\circ}-60^{\circ}$S to 20 km to 40 km which is labeled as Region 3 (R3), was characterized by positive temperature anomalies. As shown in **Figure 2**, the temperature anomalies are close to zero before the E Event (before Ls=32°) in all three regions. Shortly after the occurrence of E event E (near Ls$\approx 34^{\circ}$), the anomalous temperatures in R1 and R3 increase rapidly (with a tendency of ~ 2K/Ls near Ls=36°) and reach their maxima (9.3 K for region 1; approximately 12 K for R3) at Ls=40° and Ls$=42^{\circ}$, respectively. The positive anomalies began to decrease from Ls =44° to the end of the E Event (near Ls$=47^{\circ}$). The anomalous temperature in R2 decreased at approximately Ls≈34°, reaching its minimum of -3.2 K at approximately Ls=38°. Then, it began to rise and come back to normal at Ls=44°.

The factors impacting the temperature anomalies in these regions are examined by decomposing the heating rate into a radiative term (consisting of shortwave and longwave radiative heating rates) and a dynamic term (as shown in Equation 6). The sum of the dynamic and radiative terms in R1 (**Figure 2c**) could explain most of the temperature variation (red solid line in **Figure 2b**). The anomalous radiative heating rate (approximately 4.6 K/Ls) dominates the temperature variation, while the dynamic term tends to counteract the radiative effect with an anomalous heating rate of -2.1 K/Ls. The anomalous radiative heating increase in R1 was primarily contributed by the direct absorption of shortwave radiation by the dust. In contrast, the anomalous longwave heating was positive during the initial phase of the E Event, from Ls=33° to Ls=38°. The variations in the anomalous heating rate due to longwave radiation and the temperature in R1 are synchronous, both reaching their peak at Ls=42°, indicates that the longwave radiation emitted from tropospheric air increased as the temperature increased. As a result, the increased longwave radiation emitted from the atmosphere tended to decrease the temperature anomalies in R1 after Ls=38° (**Figure 2a and 2c**).

The weakening of the shortwave heating after Ls=49° may be attributed to the obstruction effect of the lifted dust in R1.

For Region 2 (**Figure 2d**), the dynamical term plays an important role in the cooling process, which causes an anomalous heating rate of approximately 0.9 K/Ls. As suggested by previous studies, the dynamic response can be related to atmospheric waves (such as PWs and GWs) (Battalio et al., 2022; Kuroda et al., 2020; Shaposhnikov et al., 2022), which can transport momentum by interact with the mean flow, affecting the residual circulation and the temperature (Andrews et al., 1987). As shown in Eq. (6), the dynamic heating rate from the LMD simulation can be decomposed into a resolved (PW) term and an unresolved (GW) term. The adiabatic heating from the GWs dominates the anomalous cooling in R2 from Ls$\approx 32^{\circ} - 39^{\circ}$, while the adiabatic heating due to PWs counteracts that due to GWs. During Ls$\approx 40^{\circ} - 45^{\circ}$, the dynamic heating induced by PWs and that induced by longwave radiation contributed primarily to the positive temperature anomaly. The radiative effect tends to increase the temperature anomalies in R2 at Ls $\approx$ 35°, primarily due to the influence of longwave heating.

The anomalous heating in R3 (**Figure 2e**) during the E event is mainly attributed to the dynamical effects, especially those induced by PWs. The effects of GWs on temperature anomalies counteract those of PWs before Ls$\approx 41^{\circ}$. The anomalous radiative term in R3, primarily contributed by the longwave component, tends to decrease the temperature anomalies and counteract the dynamical effect during the E event. The positive shortwave heating anomalies may be caused by direct solar heating absorption from the increased dust particles transported into R3. However, the effect of the shortwave radiation is relatively small compared with the magnitude of longwave cooling.

4. Discussions

The atmospheric wave activities are then examined based on the TEM framework to further investigate the dynamic response during this early dust event. **Figure 3** shows the EP fluxes before and during the E Event. The climatological EP flux divergence is positive in the northern troposphere (the positive EPD in **Figure 3a**), associated with downward propagation below 30 km and upward propagation above into the northern mesosphere (R2). PWs also transport from R1 to R3, where the EP flux converges (dissipates). Before the onset of the E event (approximately Ls≈32°), the anomalous EPD was centered at approximately 30°N, 60 km (**Figure 3b**), associated with the southward propagation of EP flux anomalies from 30°N to 40-50°S at 40 km and 70 km. Suppressed dissipation of PWs (positive EP flux divergence peaking at approximately 10 $\mathrm{m}/s/day$) is evident in the northern troposphere (~ 20 km), coinciding with the anomalous heating in R1 (**Figure 1c and 2c**). At the beginning of the E Event (Ls$\approx 36^{\circ}$), the downward propagation of PWs is enhanced in R1. Still, it is suppressed, accompanied by enhanced PW dissipation near R3 (**Figure 3b**).

At Ls$\approx 36^{\circ}$, the positive anomalies of the EP flux divergence in R1 begin to decrease (**Figure 3c)**. At the same time, the upward propagation of PWs into the mesosphere (40-80 km) was enhanced. The propagation of PWs across the equator is also intensified in the upper troposphere and mesosphere. In R3, there is a pronounced increase in the anomalous EPD. The dissipation of PWs in the southern troposphere suggests the transfer of westward momentum to the background zonal winds. The EP flux with a wavenumber of 1 to 3 (WN 1-3) accounts for most of the total EP flux anomalies (**Figure 4a)**. The WN1 component dominates the EP flux anomalies in R2 and southern middle latitudes (near the surface to the mesopause) **(Figure 4b**). In contrast, the WN2 component mainly contributes to the EP flux anomalies in R1 (**Figure 4c**). The WN3 component plays an important role in R3 (**Figure 4d**).

The zonal mean zonal wind anomalies during the E event, along with the anomalous EPD and GWs drag, are shown in **Figure 5.** The positive EPD leads to enhanced eastward zonal wind anomalies in the lower (~20 km) northern troposphere (**Figure 5a**). The zonal mean zonal wind anomalies are eastward in the tropical (-$30^{\circ} - 30^{\circ}$N) troposphere (20 km) and the lower mesosphere region (up to 60 km).

In the middle- and high-latitude regions, the zonal mean zonal wind anomalies are westward in the troposphere and mesosphere of both hemispheres. The negative EPD anomalies in R3 tend to suppress the eastward background wind (the zonal wind anomalies are -10 m/s in the tropopause). Due to the quasi-geostrophic balance, the meridional circulation anomalies become southward in the southern hemisphere, which further cause the anomalous downwelling and modulate the temperature via the adiabatic process in R3 (Figure 6).

The positive EPD anomalies near the equator are responsible for the enhanced eastward wind anomalies. As presented in **Figure 6**, there is anomalous upwelling in the residual circulation in R1, which tends to counteract the radiative heating due to the adiabatic cooling (**Figure 2c)**. Besides the effect of PWs, GWs also play a role in the modulation of the zonal wind and temperature in the mesosphere region (Alexander et al., 2011; Vincent, 1987). The negative GW drag (GWD) anomalies in R1 (indicating the westward momentum anomalies) and in the tropical mesosphere tend to suppress the eastward wind, which counteracts the effect of the PWs (**Figure 5b**). Due to the critical level filtering (Fritts & Alexander, 2003), the enhanced eastward background flow in R1 would increase eastward GWs' absorption, increasing the westward net momentum in the upper atmosphere (R2). In the tropical region, the anomalous GWD provides eastward momentum in the tropical tropopause region (~40 km) with an amplitude of approximately 1.3 m/s/day. As a result of the eastward wind anomalies in the tropical tropopause region, the westward GW drag increased (negative anomalies) in the tropical mesosphere (**Figure 5b**). The EPD generally dominates the anomalous momentum budget in the troposphere, while the GWD contributes more momentum anomalies in the mesosphere.

As the anomalous residual circulation can also affect the transportation of water vapor, the total water column mass flux across the equator is calculated as described in equation (7) from Ls= 25°-47° to verify the potential impact of dust storm on the water budget in the first half of MY35. As shown in **Figure 7a** and **7b**, water transport across the equator is simulated by LMD considering both water ice and water vapor mass flux components. The mass flux of water is mainly from the water ice transport in both the climatological case and the MY35 case, since the Martian atmosphere is cold and cloudy near the aphelion (Clancy et al., 2021; Guha et al., 2021b; J. -B. Madeleine, Forget, Spiga, et al., 2012). The water column mass flux is smaller than $1 \times 10^4\ kg/s$ within the same Ls range as the E Event in the climatological case. In the MY35 simulation **(Figure 7b)**, the meridional water ice mass flux across the equator was also relatively low (below $2.5 \times 10^4\ kg/s$) before the E Event (Ls=32°), while the northward water vapor mass flux was larger (at $1.8 \times 10^4\ kg/s$) than that in the climatological case.

Following the development of dust storm in the northern hemisphere, the northward water vapor flux became negative after the occurrence of the E event (Ls = 32°). It reached its minimum of approximately -7.2×10^4kg/s at Ls≈ 40° (**Figure 7b**), indicating significant southward water vapor transport coincides with the anomalous southward residual meridional mean circulation. As the E event further developed (Ls≈ $42^{\circ} - 45^{\circ}$), the northward water mass flux became positive again with a magnitude of approximately 2.3×10^4kg/s. Although the direction of the meridional transport of water altered throughout the evolution of the E event, the net transport of water toward the southern hemisphere remained significant. As a result, this increased southward transfer of water (6.8975×10^{10} kg) accounts for nearly 35.9% of the net interhemispheric water transport (from northern to southern hemisphere) in an entire Martian year. The increased water transport into the southern hemisphere during the E event significantly affects Mars's annual water vapor cycle, potentially affecting the water cycle and escape in the latter half of the Martian year. (Fedorova et al., 2018; Heavens et al., 2018; Stone et al., 2020; Sun et al., 2023; Wu et al., 2020).

5. Summary

This study reported a rarely occurring dust storm during the low dust loading season in MY 35. Anomalous warming occurred in the midlatitude troposphere of both hemispheres (R1 and R3), and anomalous cooling occurred in the northern mesosphere (R2). The LMD simulations with the MY35 dust scenario reproduce similar temperature anomalies during the E event. Direct heating (shortwave) from dust absorption dominates the temperature variation in R1 during the E event. With the help of the TEM analysis framework, heating sources from different physical processes, including dynamic and radiative effects, were investigated. The PWs propagated from the dust-rich region in the northern troposphere to the southern hemisphere during the E event. The increased dissipation of PWs in R3 could enhance the residual meridional circulation, which further cause the temperature warming in R3 via the adiabatic heating. The heating rate from the dynamical terms (mainly from EPD/PWs) tends to decrease the temperature in R1 following the upwelling residual circulation (adiabatic cooling).

As the anomalous EDP provides eastward (positive) momentum to the zonal wind in the troposphere (R1), more eastward GWs are absorbed in that region due to the critical level filtering. The upward net westward momentum by the GWs further modulates the residual circulation in the northern mesosphere and leads to adiabatic cooling in R2, which is similar to the vertical coupling dynamic mechanisms on Earth (Becker, 2012; Karlsson et al., 2007, 2009; Li et al., 2016; Murphy et al., 2012).

Consistent with the enhanced north-to-south flow, the net meridional transport of water from north to south increases during the E event, as revealed by the LMD simulations. The enhanced residual circulation significantly strengthens the net interhemispheric water transport by 35.92% compared to the total net water transport during an entire Martian year. These anomalous water transports could increase water storage in the Southern Hemisphere, which potentially affects the annual water cycle and water escape during the high dust loading season during the Southern Hemisphere summer season (Fedorova et al., 2018; Heavens et al., 2018; Wu et al., 2020).

Acknowledgments

This work was supported by the B-type Strategic Priority Program of the Chinese Academy of Sciences, grant no. XDB41000000; the National Natural Science Foundation of China, grants 42241115, 42275133, 42130203; the National Key R&D Program of China, grant no. 2022YFF0503703.

Data Availability Statement

The observation data of the MCS mentioned in this study can be found on the Planetary Atmospheres Node (ATM) of the Planetary Data System (PDS) at https://pds-atmospheres.nmsu.edu/data_and_services/atmospheres_data/MARS/atmosphere_temp_prof.html. The derived MCS data and LMD simulation results presented in this study have been archived on the OSF repository https://doi.org/10.17605/OSF.IO/CDPGU (Sun et al., 2023).

Figure Captions

Figure 1. The zonal mean total column dust opacity depth from Ls= 0-90° (a); the black dotted lines show the reference time range of the E Event. The zonal mean density scaled opacity depth anomalies from the MCS observations (c) and the zonal mean mass mixing ratio anomalies from the LMD simulations (e); the zonal mean temperature anomalies during the E Event from MCS observations (d) and LMD simulations (d) at Ls=36° (the development stage of the E Event). The contour interval in (b) and (c) is 1 K. The gray filled-in area refers to the missing data or the level underground.

Figure 2. The temperature anomalies (shadings) with rectangles are labeled region 1 (heating region in the troposphere at the northern middle latitudes), region 2 (cooling region in the lower mesosphere at the northern middle latitudes), and region 3 (heating region in the upper troposphere at the southern middle latitudes) (a). The regional mean temperature anomaly variations during the E Event period are shown in (b). The solid jacinth line represents the regional mean temperature anomalies in

region 1, the solid light blue line represents the regional mean temperature anomalies in region 2, and the solid purple line represents the regional mean temperature anomalies in region 3. The heating rate decompositions of region 1 (c), region 2 (d) and region 3 (e) are shown with solid black lines representing the summations of the heating rate from dynamic and radiative processes, while the bold dashed lines with the same color as in (b) represent the temporal variation in the temperature in the corresponding region. The solid green lines represent the heating rates from the dynamic processes, the solid red line represents the heating rates from the radiative processes, the dotted blue lines represent the dynamic heating rates from PWs, and the dotted red lines represent the dynamic heating rates from GWs. The dotted light green lines represent the heating rates from longwave radiation, and the dotted blue lines represent the heating rates from shortwave radiation.

Figure 3. The EP flux (quivers) and its divergence (shadings) in the climatological case during the same time period as the E event (Ls$\approx 32^{\circ} - 45^{\circ}$) (a), during the initial stage (Ls$\approx 32^{\circ}$) (b) and during the development stage (Ls$\approx 36^{\circ}$) (c).

Figure 4. The EP flux (quivers) and its divergence (shadings) from the WN1-3 sum (a), WN1 component (b), WN2 component (c) and WN3 component (d) at Ls=36°.

Figure 5. The zonal mean zonal wind (contour lines) along with the EPD (a) and parameterized GWD (b) (shading) at Ls=36°. The contour interval is 5 m/s.

Figure 6. The residual circulation anomalies in the initial stage (Ls=32°) (a) and development stage (Ls=36°) (b) of the E Event (quivers) along with zonal mean temperature anomalies (shadings).

Figure 7. The total column water mass transport variation from the Northern to Southern Hemisphere in the climatological case (a) and the MY35 case (b). The blue lines represent the water mass transport of water ice, the red lines represent the water mass transport of water vapor, and the black lines are the summations of the water components.

Figures

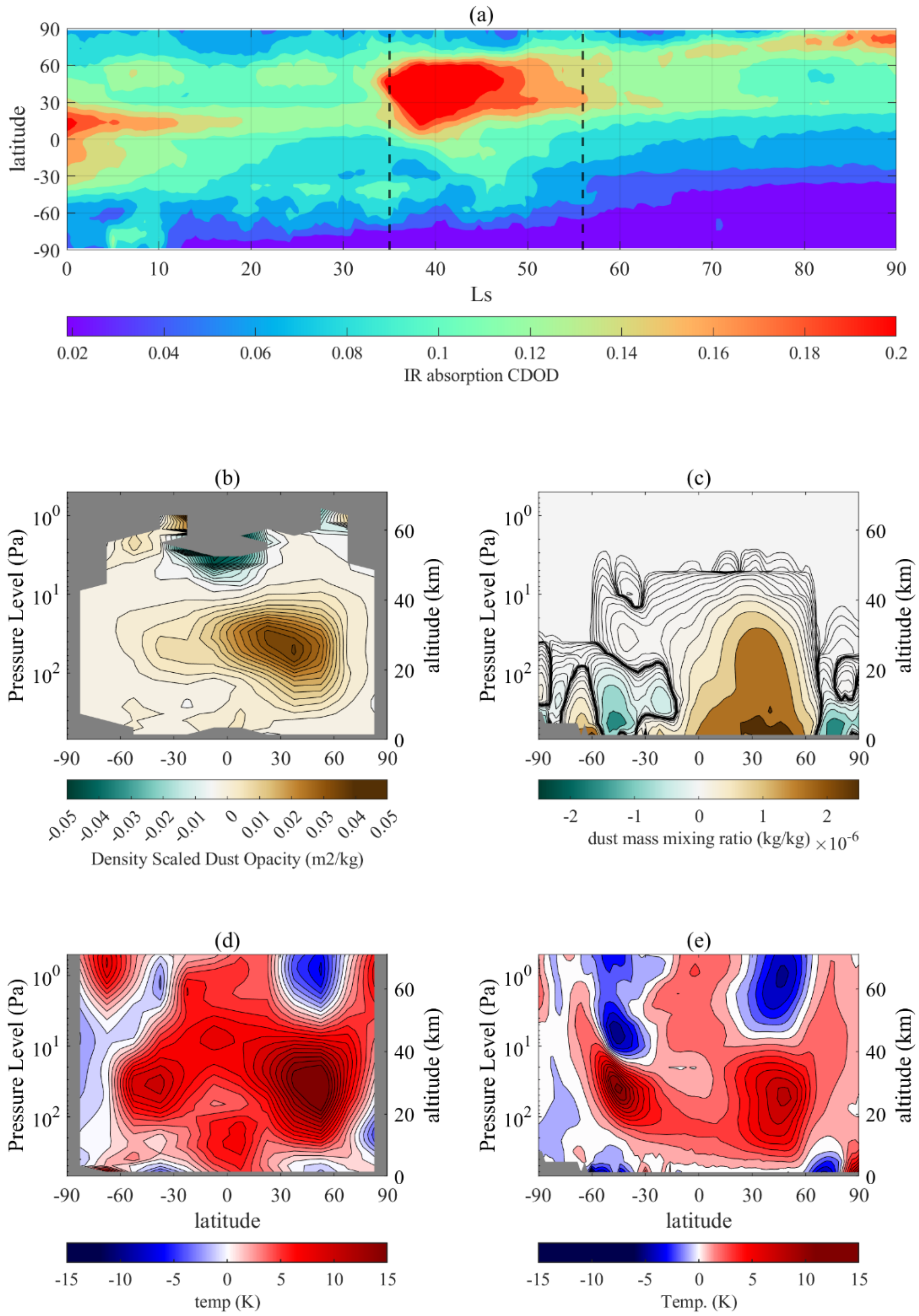

Figure 1. The zonal mean total column dust opacity depth from Ls= 0-90° (a); the black dotted lines show the reference time range of the E Event. The zonal mean density scaled opacity depth anomalies from the MCS observations (c) and the zonal mean mass mixing ratio anomalies from the LMD simulations (e); the zonal mean temperature anomalies during the E Event from MCS observations (d) and LMD simulations (d) at Ls=36° (the development stage of the E Event). The contour

interval in (b) and (c) is 1 K. The gray filled-in area refers to the missing data or the level underground.

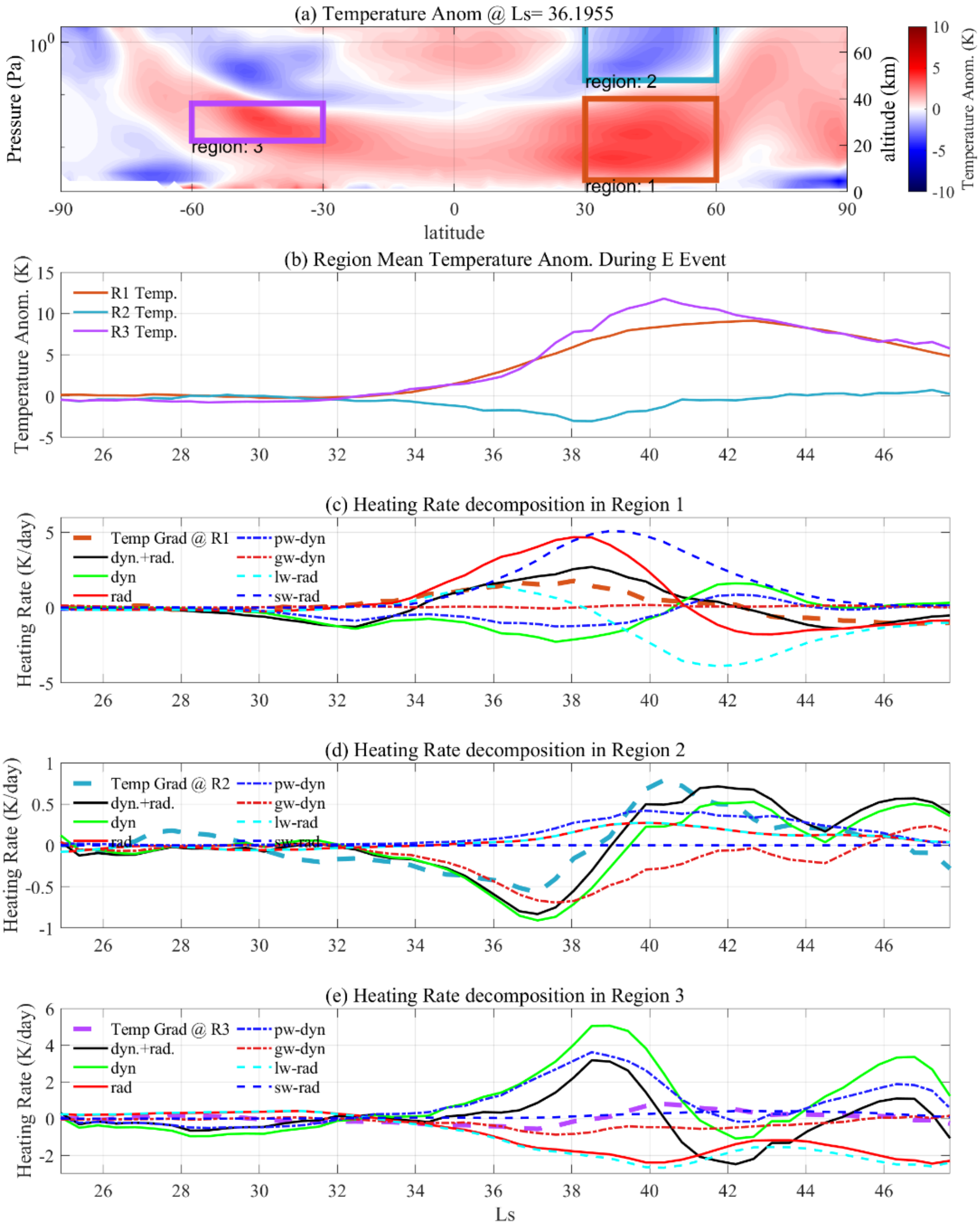

Figure 2. The temperature anomalies (shadings) with rectangles are labeled region 1 (heating region in the troposphere at the northern middle latitudes), region 2 (cooling region in the lower mesosphere at the northern middle latitudes), and region 3 (heating region in the upper troposphere at the southern middle latitudes) (a). The regional mean temperature anomaly variations during the E Event period are shown in

(b). The solid jacinth line represents the regional mean temperature anomalies in region 1, the solid light blue line represents the regional mean temperature anomalies in region 2, and the solid purple line represents the regional mean temperature anomalies in region 3. The heating rate decompositions of region 1 (c), region 2 (d) and region 3 (e) are shown with solid black lines representing the summations of the heating rate from dynamic and radiative processes, while the bold dashed lines with the same color as in (b) represent the temporal variation in the temperature in the corresponding region. The solid green lines represent the heating rates from the dynamic processes, the solid red line represents the heating rates from the radiative processes, the dotted blue lines represent the dynamic heating rates from PWs, and the dotted red lines represent the dynamic heating rates from GWs. The dotted light green lines represent the heating rates from longwave radiation, and the dotted blue lines represent the heating rates from shortwave radiation.

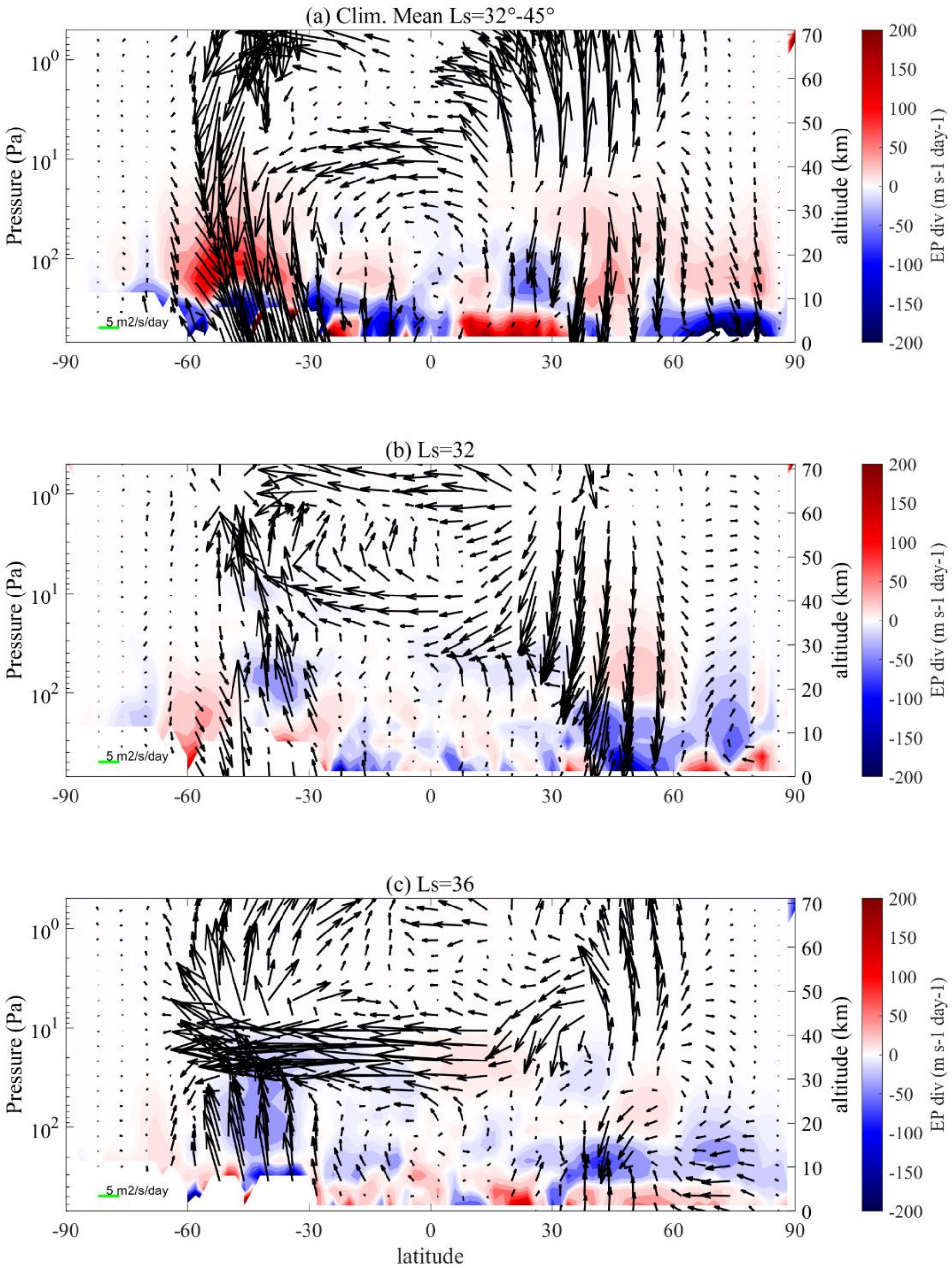

Figure 3. The EP flux (quivers) and its divergence (shadings) in the climatological case during the same time period as the E event (Ls$\approx 32^{\circ} - 45^{\circ}$) (a), during the initial stage (Ls$\approx 32^{\circ}$) (b) and during the development stage (Ls$\approx 36^{\circ}$) (c).

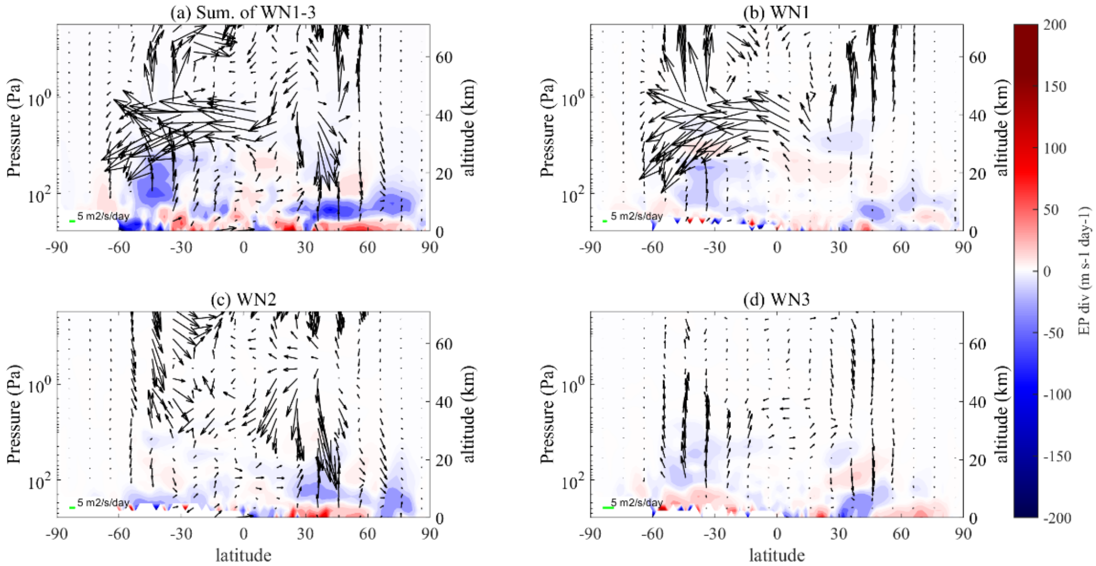

Figure 4. The EP flux (quivers) and its divergence (shadings) from the WN1-3 sum (a), WN1 component (b), WN2 component (c) and WN3 component (d) at Ls=36°.

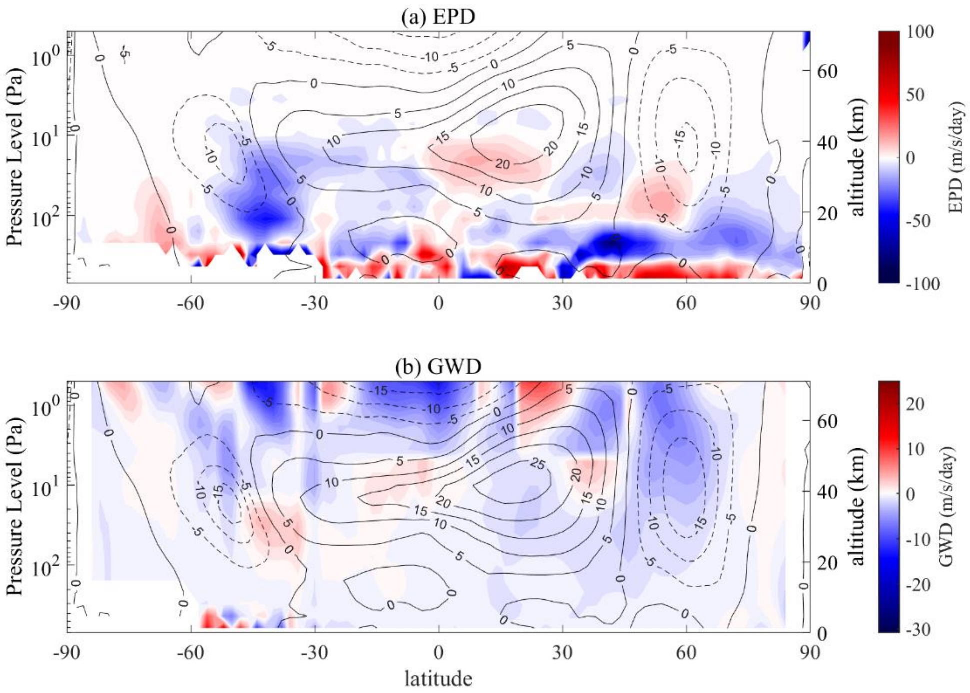

Figure 5. The zonal mean zonal wind anomalies (contour lines) along with the EPD (a) and parameterized GWD (b) (shading) at Ls=36°. The contour interval is 5 m/s.

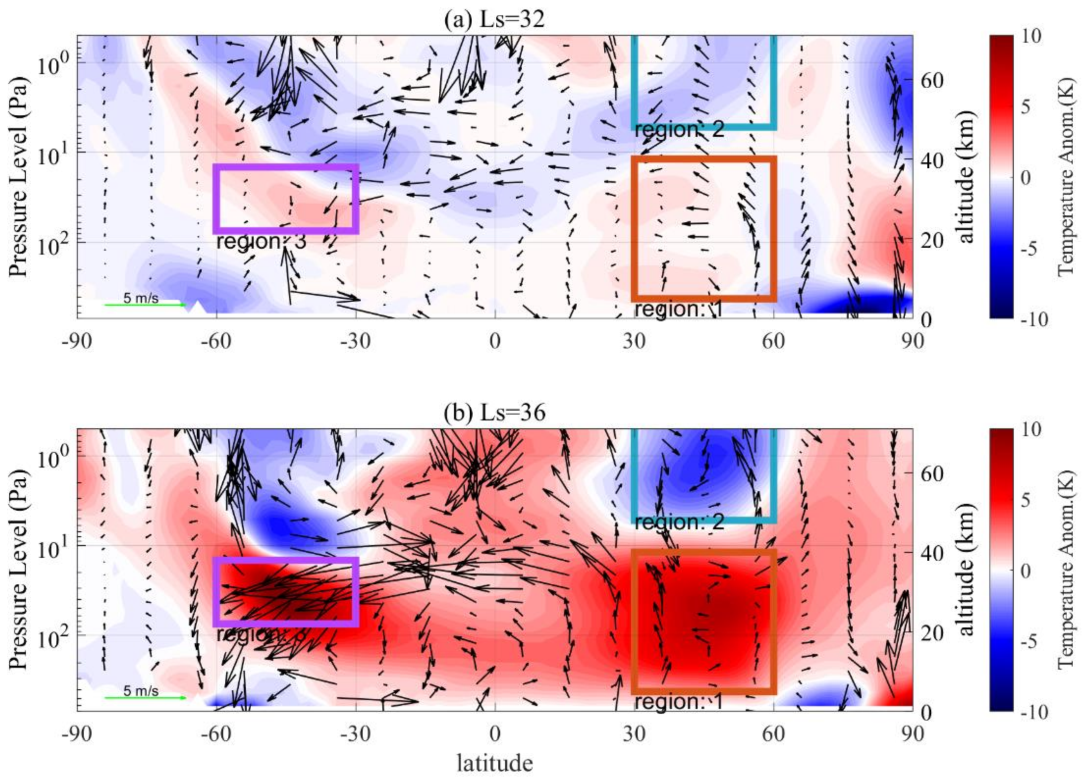

Figure 6. The residual circulation anomalies in the initial stage (Ls=32°) (a) and development stage (Ls=36°) (b) of the E Event (quivers) along with zonal mean temperature anomalies (shadings).

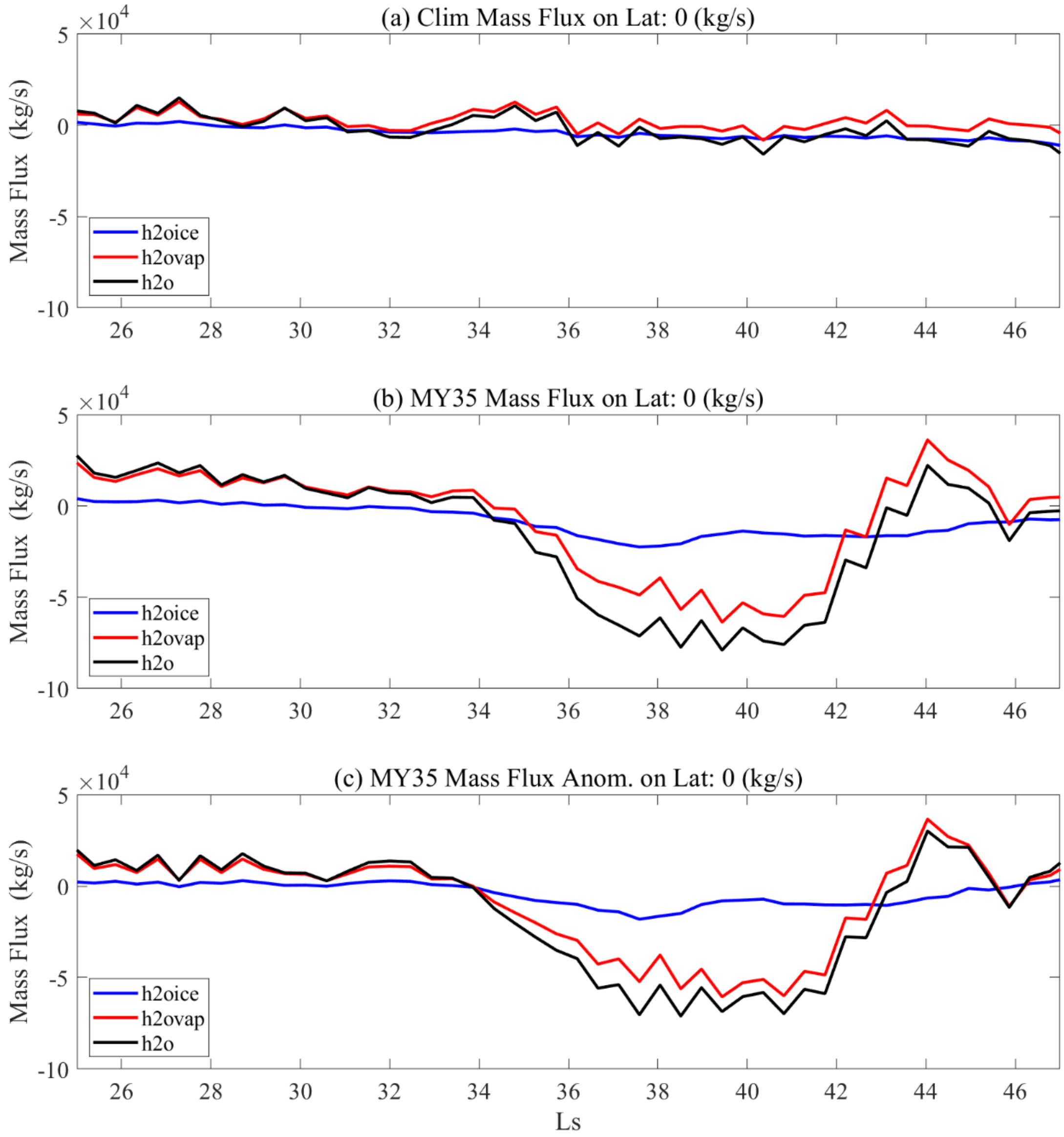

Figure 7. The total column water mass transport variation from the Northern to Southern Hemisphere in the climatological case (a) and the MY35 case (b). The blue lines represent the water mass transport of water ice, the red lines represent the water mass transport of water vapor, and the black lines are the summations of the water components.

References

Alexander, S. P., Klekociuk, A. R., & Murphy, D. J. (2011). Rayleigh lidar observations of gravity wave activity in the winter upper stratosphere and lower mesosphere above Davis, Antarctica (69°S, 78°E). *Journal of Geophysical Research*, *116*(D13), D13109. https://doi.org/10.1029/2010JD015164

Andrews, D. G. (1987). On the interpretation of the eliassen-palm flux divergence. *Quarterly Journal of the Royal Meteorological Society*, *113*(475), 323–338. https://doi.org/10.1002/qj.49711347518

Andrews, D. G., Holton, J. R., & Leovy, C. B. (1987). *Middle atmosphere dynamics* (Issue 40). Academic press.

Battalio, J. M., Martínez, G., Newman, C., De La Torre Juarez, M., Sánchez-Lavega, A., & Víudez-Moreiras, D. (2022). Planetary Waves Traveling Between Mars Science Laboratory and Mars 2020. *Geophysical Research Letters*, *49*(21), e2022GL100866. https://doi.org/10.1029/2022GL100866

Becker, E. (2012). Dynamical Control of the Middle Atmosphere. *Space Science Reviews*, *168*(1–4), 283–314. https://doi.org/10.1007/s11214-011-9841-5

Cantor, B. A. (2007). MOC observations of the 2001 Mars planet-encircling dust storm. *Icarus*, *186*(1), 60–96. https://doi.org/10.1016/j.icarus.2006.08.019

Cantor, B. A., James, P. B., Caplinger, M., & Wolff, M. J. (2001). Martian dust storms: 1999 Mars Orbiter Camera observations. *Journal of Geophysical Research: Planets*, *106*(E10), 23653–23687. https://doi.org/10.1029/2000JE001310

Clancy, R. T., Wolff, M. J., Heavens, N. G., James, P. B., Lee, S. W., Sandor, B. J., Cantor, B. A., Malin, M. C., Tyler, D., & Spiga, A. (2021). Mars perihelion cloud trails as revealed by MARCI: Mesoscale topographically focused updrafts and gravity wave forcing of high altitude clouds. *Icarus*, *362*, 114411. https://doi.org/10.1016/j.icarus.2021.114411

Colaïtis, A., Spiga, A., Hourdin, F., Rio, C., Forget, F., & Millour, E. (2013). A thermal plume model for the Martian convective boundary layer. *Journal of Geophysical Research: Planets*, *118*(7), 1468–1487. https://doi.org/10.1002/jgre.20104

Creasey, J. E., Forbes, J. M., & Hinson, D. P. (2006). Global and seasonal distribution of gravity wave activity in Mars' lower atmosphere derived from MGS radio occultation data. *Geophysical Research Letters*, *33*(1), 2005GL024037. https://doi.org/10.1029/2005GL024037

Dunkerton, T., Hsu, C.-P. F., & McIntyre, M. E. (1981). Some Eulerian and Lagrangian Diagnostics for a Model Stratospheric Warming. *Journal of the Atmospheric Sciences*, *38*(4), 819–844. https://doi.org/10.1175/1520-0469(1981)038<0819:SEALDF>2.0.CO;2

Fang, X., Ma, Y., Lee, Y., Bougher, S., Liu, G., Benna, M., Mahaffy, P., Montabone, L., Pawlowski, D., Dong, C., Dong, Y., & Jakosky, B. (2020). Mars Dust Storm Effects in the Ionosphere and Magnetosphere and Implications for Atmospheric Carbon Loss. *Journal of Geophysical Research: Space Physics*, *125*(3), e2019JA026838. https://doi.org/10.1029/2019JA026838

Fedorova, A., Bertaux, J.-L., Betsis, D., Montmessin, F., Korablev, O., Maltagliati, L., & Clarke, J. (2018). Water vapor in the middle atmosphere of Mars during the 2007 global dust storm. *Icarus*, *300*, 440–457. https://doi.org/10.1016/j.icarus.2017.09.025

Forget, F. (1998). Improved optical properties of the Martian atmospheric dust for radiative transfer calculations in the infrared. *Geophysical Research Letters*, *25*(7), 1105–1108. https://doi.org/10.1029/98GL50653

Forget, F., Hourdin, F., Fournier, R., Hourdin, C., Talagrand, O., Collins, M., Lewis, S. R., Read, P. L., & Huot, J. (1999). Improved general circulation models of the Martian atmosphere from the surface to above 80 km. *Journal of Geophysical Research: Planets*, *104*(E10), 24155–24175. https://doi.org/10.1029/1999JE001025

Fritts, D. C., & Alexander, M. J. (2003). Gravity wave dynamics and effects in the middle atmosphere. *Reviews of Geophysics*, *41*(1), 2001RG000106. https://doi.org/10.1029/2001RG000106

Gilli, G., Forget, F., Spiga, A., Navarro, T., Millour, E., Montabone, L., Kleinböhl, A., Kass, D. M., McCleese, D. J., & Schofield, J. T. (2020). Impact of Gravity Waves on the Middle Atmosphere of Mars: A Non-Orographic Gravity Wave Parameterization Based on Global Climate Modeling and MCS Observations. *Journal of Geophysical Research: Planets*, *125*(3), e2018JE005873. https://doi.org/10.1029/2018JE005873

Girazian, Z., Luppen, Z., Morgan, D. D., Chu, F., Montabone, L., Thiemann, E. M. B., Gurnett, D. A., Halekas, J., Kopf, A. J., & Němec, F. (2020). Variations in the Ionospheric Peak Altitude at Mars in Response to Dust Storms: 13 Years of Observations From the Mars Express Radar Sounder. *Journal of Geophysical Research: Planets*, *125*(5), e2019JE006092. https://doi.org/10.1029/2019JE006092

Guha, B. K., Panda, J., & Wu, Z. (2021a). Observation of aphelion cloud belt over Martian tropics, its evolution, and associated dust distribution from MCS data. *Advances in Space Research*, *67*(4), 1392–1411. https://doi.org/10.1016/j.asr.2020.11.010

Guha, B. K., Panda, J., & Wu, Z. (2021b). Observation of aphelion cloud belt over Martian tropics, its evolution, and associated dust distribution from MCS data. *Advances in Space Research*, *67*(4), 1392–1411. https://doi.org/10.1016/j.asr.2020.11.010

Guzewich, S. D., Toigo, A. D., & Waugh, D. W. (2016). The effect of dust on the martian polar vortices. *Icarus*, *278*, 100–118. https://doi.org/10.1016/j.icarus.2016.06.009

Haberle, R. M., Clancy, R. T., Forget, F., Smith, M. D., & Zurek, R. W. (Eds.). (2017). *The Atmosphere and Climate of Mars* (1st ed.). Cambridge University Press. https://doi.org/10.1017/9781139060172

Heavens, N. G., Kleinböhl, A., Chaffin, M. S., Halekas, J. S., Kass, D. M., Hayne, P. O., McCleese, D. J., Piqueux, S., Shirley, J. H., & Schofield, J. T. (2018). Hydrogen escape from Mars enhanced by deep convection in dust storms. *Nature Astronomy*, *2*(2), 126–132. https://doi.org/10.1038/s41550-017-0353-4

Heavens, N. G., Richardson, M. I., Kleinböhl, A., Kass, D. M., McCleese, D. J., Abdou, W., Benson, J. L., Schofield, J. T., Shirley, J. H., & Wolkenberg, P. M. (2011). The vertical distribution of dust in the Martian atmosphere during northern spring and summer: Observations by the Mars Climate Sounder and analysis of zonal average vertical dust profiles. *Journal of Geophysical Research*, *116*(E4), E04003. https://doi.org/10.1029/2010JE003691

Huang, J., Wu, Z., Cui, J., Hao, Y., & Cao, W. (2022). Topographic Gravity Waves Observed in the Martian Thermosphere: A Statistical Perspective From a 1-D Full-Wave Model. *Journal of Geophysical Research: Space Physics*, *127*(9), e2022JA030846. https://doi.org/10.1029/2022JA030846

Kahre, M. A., Murphy, J. R., Newman, C. E., Wilson, R. J., Cantor, B. A., Lemmon, M. T., & Wolff, M. J. (2017). The Mars Dust Cycle. In R. M. Haberle, R. T. Clancy, F. Forget, M. D. Smith, & R. W. Zurek (Eds.), *The Atmosphere and Climate of Mars* (1st ed., pp. 295–337). Cambridge University Press. https://doi.org/10.1017/9781139060172.010

Karlsson, B., Körnich, H., & Gumbel, J. (2007). Evidence for interhemispheric stratosphere-mesosphere coupling derived from noctilucent cloud properties. *Geophysical Research Letters*, *34*(16), 2007GL030282. https://doi.org/10.1029/2007GL030282

Karlsson, B., McLandress, C., & Shepherd, T. G. (2009). Inter-hemispheric mesospheric coupling in a comprehensive middle atmosphere model. *Journal of Atmospheric and Solar-Terrestrial Physics*, *71*(3–4), 518–530. https://doi.org/10.1016/j.jastp.2008.08.006

Kass, D. M., Kleinböhl, A., Kass, D. M., Diego, S., & Heavens, N. G. (n.d.). *OBSERVATIONS OF THE MARS YEAR 35 E (EARLY) LARGE-SCALE REGIONAL DUST EVENT*.

Kass, D. M., Kleinböhl, A., McCleese, D. J., Schofield, J. T., & Smith, M. D. (2016). Interannual similarity in the Martian atmosphere during the dust storm season. *Geophysical Research Letters*, *43*(12), 6111–6118. https://doi.org/10.1002/2016GL068978

Keeble, J., Braesicke, P., Abraham, N. L., Roscoe, H. K., & Pyle, J. A. (2014). The impact of polar stratospheric ozone loss on Southern Hemisphere stratospheric circulation and climate. *Atmospheric Chemistry and Physics*, *14*(24), 13705–13717. https://doi.org/10.5194/acp-14-13705-2014

Kleinböhl, A., John Wilson, R., Kass, D., Schofield, J. T., & McCleese, D. J. (2013). The semidiurnal tide in the middle atmosphere of Mars. *Geophysical Research Letters*, *40*(10), 1952–1959. https://doi.org/10.1002/grl.50497

Kleinböhl, A., Schofield, J. T., Kass, D. M., Abdou, W. A., Backus, C. R., Sen, B., Shirley, J. H., Lawson, W. G., Richardson, M. I., Taylor, F. W., Teanby, N. A., & McCleese, D. J. (2009). Mars Climate Sounder limb profile retrieval of atmospheric temperature, pressure, and dust and water ice opacity. *Journal of Geophysical Research: Planets*, *114*(E10), 2009JE003358. https://doi.org/10.1029/2009JE003358

Kuroda, T., Medvedev, A. S., & Yiğit, E. (2020). Gravity Wave Activity in the Atmosphere of Mars During the 2018 Global Dust Storm: Simulations With a High-Resolution Model. *Journal of Geophysical Research: Planets*, *125*(11), e2020JE006556. https://doi.org/10.1029/2020JE006556

Lee, C., Lawson, W. G., Richardson, M. I., Heavens, N. G., Kleinböhl, A., Banfield, D., McCleese, D. J., Zurek, R., Kass, D., Schofield, J. T., Leovy, C. B., Taylor, F. W., & Toigo, A. D. (2009). Thermal tides in the Martian middle atmosphere as seen by the Mars Climate Sounder. *Journal of Geophysical Research: Planets*, *114*(E3), 2008JE003285. https://doi.org/10.1029/2008JE003285

Li, J., Wu, Z., Li, T., Zhang, X., Cui, J., Planetary Environmental and Astrobiological Research Laboratory, School of Atmospheric Sciences, Sun Yat-sen University, Zhuhai Guangdong 519082, China, Chinese Academy of Sciences Key Laboratory of Geospace Environment, School of Earth and Space Sciences, University of Science and Technology of China, Hefei 230026, China, Department of Earth and Planetary Sciences, University of California Santa Cruz, Santa Cruz, California 95064, USA, Chinese Academy of Sciences Key Laboratory of Lunar and Deep Space Exploration, National Astronomical Observatories, Chinese Academy of Sciences, Beijing 100012, China, & Chinese

Academy of Sciences Center for Excellence in Comparative Planetology, Hefei 230026, China. (2020). The diurnal transport of atmospheric water vapor during major dust storms on Mars based on the Mars Climate Database, version 5.3. *Earth and Planetary Physics*, *4*(6), 550–564. https://doi.org/10.26464/epp2020062

Li, T., Calvo, N., Yue, J., Russell, J. M., Smith, A. K., Mlynczak, M. G., Chandran, A., Dou, X., & Liu, A. Z. (2016). Southern Hemisphere Summer Mesopause Responses to El Niño–Southern Oscillation. *Journal of Climate*, *29*(17), 6319–6328. https://doi.org/10.1175/JCLI-D-15-0816.1

Liu, J., Millour, E., Forget, F., Gilli, G., Lott, F., Bardet, D., González Galindo, F., Bierjon, A., Naar, J., Martinez, A., Lebonnois, S., Fan, S., Pierron, T., & Vandemeulebrouck, R. (2023). A Surface to Exosphere Non-Orographic Gravity Wave Parameterization for the Mars Planetary Climate Model. *Journal of Geophysical Research: Planets*, *128*(7), e2023JE007769. https://doi.org/10.1029/2023JE007769

Liuzzi, G., Villanueva, G. L., Crismani, M. M. J., Smith, M. D., Mumma, M. J., Daerden, F., Aoki, S., Vandaele, A. C., Clancy, R. T., Erwin, J., Thomas, I., Ristic, B., Lopez-Moreno, J., Bellucci, G., & Patel, M. R. (2020). Strong Variability of Martian Water Ice Clouds During Dust Storms Revealed From ExoMars Trace Gas Orbiter/NOMAD. *Journal of Geophysical Research: Planets*, *125*(4), e2019JE006250. https://doi.org/10.1029/2019JE006250

Lott, F., & Millet, C. (2010). The Representation of Gravity Waves in Atmospheric General Circulation Models (GCMs). In A. Le Pichon, E. Blanc, & A. Hauchecorne (Eds.), *Infrasound Monitoring for Atmospheric Studies* (pp. 685–699). Springer Netherlands.

https://doi.org/10.1007/978-1-4020-9508-5_23

Määttänen, A., & Montmessin, F. (2021). Clouds in the Martian Atmosphere. In A. Määttänen & F. Montmessin, *Oxford Research Encyclopedia of Planetary Science*. Oxford University Press. https://doi.org/10.1093/acrefore/9780190647926.013.114

Madeleine, J. -B., Forget, F., Millour, E., Navarro, T., & Spiga, A. (2012). The influence of radiatively active water ice clouds on the Martian climate. *Geophysical Research Letters*, *39*(23), 2012GL053564. https://doi.org/10.1029/2012GL053564

Madeleine, J. -B., Forget, F., Spiga, A., Wolff, M. J., Montmessin, F., Vincendon, M., Jouglet, D., Gondet, B., Bibring, J. -P., Langevin, Y., & Schmitt, B. (2012). Aphelion water-ice cloud mapping and property retrieval using the OMEGA imaging spectrometer onboard Mars Express. *Journal of Geophysical Research: Planets*, *117*(E11), 2011JE003940. https://doi.org/10.1029/2011JE003940

Madeleine, J. -B., Head, J. W., Forget, F., Navarro, T., Millour, E., Spiga, A., Colaïtis, A., Määttänen, A., Montmessin, F., & Dickson, J. L. (2014). Recent Ice Ages on Mars: The role of radiatively active clouds and cloud microphysics. *Geophysical Research Letters*, *41*(14), 4873–4879. https://doi.org/10.1002/2014GL059861

Madeleine, J.-B., Forget, F., Millour, E., Montabone, L., & Wolff, M. J. (2011). Revisiting the radiative impact of dust on Mars using the LMD Global Climate Model. *Journal of Geophysical Research*, *116*(E11), E11010. https://doi.org/10.1029/2011JE003855

Mateshvili, N., Fussen, D., Vanhellemont, F., Bingen, C., Dodion, J., Montmessin, F., Perrier, S., Dimarellis, E., & Bertaux, J. (2007). Martian ice cloud distribution obtained from SPICAM nadir UV measurements. *Journal of Geophysical Research: Planets*, *112*(E7), 2006JE002827. https://doi.org/10.1029/2006JE002827

McCleese, D. J., Schofield, J. T., Taylor, F. W., Calcutt, S. B., Foote, M. C., Kass, D. M., Leovy, C. B., Paige, D. A., Read, P. L., & Zurek, R. W. (2007). Mars Climate Sounder: An investigation of thermal and water vapor structure, dust and condensate distributions in the atmosphere, and energy balance of the polar regions. *Journal of Geophysical Research: Planets*, *112*(E5), 2006JE002790. https://doi.org/10.1029/2006JE002790

Montabone, L., Forget, F., Millour, E., Wilson, R. J., Lewis, S. R., Cantor, B., Kass, D., Kleinböhl, A., Lemmon, M. T., Smith, M. D., & Wolff, M. J. (2015). Eight-year climatology of dust optical depth on Mars. *Icarus*, *251*, 65–95. https://doi.org/10.1016/j.icarus.2014.12.034

Montabone, L., Spiga, A., Kass, D. M., Kleinböhl, A., Forget, F., & Millour, E. (2020). Martian Year 34 Column Dust Climatology from Mars Climate Sounder Observations: Reconstructed Maps and Model Simulations. *Journal of Geophysical Research: Planets*, *125*(8). https://doi.org/10.1029/2019JE006111

Montmessin, F., Forget, F., Rannou, P., Cabane, M., & Haberle, R. M. (2004). Origin and role of water ice clouds in the Martian water cycle as inferred from a general circulation model. *Journal of Geophysical Research: Planets*, *109*(E10), 2004JE002284. https://doi.org/10.1029/2004JE002284

Montmessin, F., Rannou, P., & Cabane, M. (2002). New insights into Martian dust distribution and water-ice cloud microphysics. *Journal of Geophysical Research: Planets*, *107*(E6). https://doi.org/10.1029/2001JE001520

Murphy, D. J., Alexander, S. P., & Vincent, R. A. (2012). Interhemispheric dynamical coupling to the southern mesosphere and lower thermosphere. *Journal of Geophysical Research:*

Atmospheres, *117*(D8), 2011JD016865. https://doi.org/10.1029/2011JD016865

Navarro, T., Madeleine, J.-B., Forget, F., Spiga, A., Millour, E., Montmessin, F., & Määttänen, A. (2014). Global climate modeling of the Martian water cycle with improved microphysics and radiatively active water ice clouds. *Journal of Geophysical Research: Planets*, *119*(7), 1479–1495. https://doi.org/10.1002/2013JE004550

Orr, A., Bracegirdle, T. J., Hosking, J. S., Feng, W., Roscoe, H. K., & Haigh, J. D. (2012). Strong Dynamical Modulation of the Cooling of the Polar Stratosphere Associated with the Antarctic Ozone Hole. *Journal of Climate*, *26*(2), 662–668. https://doi.org/10.1175/JCLI-D-12-00480.1

Orr, A., Bracegirdle, T. J., Hosking, J. S., Jung, T., Haigh, J. D., Phillips, T., & Feng, W. (2012). Possible Dynamical Mechanisms for Southern Hemisphere Climate Change due to the Ozone Hole. *Journal of the Atmospheric Sciences*, *69*(10), 2917–2932. https://doi.org/10.1175/JAS-D-11-0210.1

Shaposhnikov, D. S., Medvedev, A. S., Rodin, A. V., Yiğit, E., & Hartogh, P. (2022). Martian Dust Storms and Gravity Waves: Disentangling Water Transport to the Upper Atmosphere. *Journal of Geophysical Research: Planets*, *127*(1), e2021JE007102. https://doi.org/10.1029/2021JE007102

Stone, S. W., Yelle, R. V., Benna, M., Lo, D. Y., Elrod, M. K., & Mahaffy, P. R. (2020). Hydrogen escape from Mars is driven by seasonal and dust storm transport of water. *Science*, *370*(6518), 824–831. https://doi.org/10.1126/science.aba5229

Streeter, P. M., Lewis, S. R., Patel, M. R., Holmes, J. A., Fedorova, A. A., Kass, D. M., & Kleinböhl, A. (2021). Asymmetric Impacts on Mars' Polar Vortices From an Equinoctial

Global Dust Storm. *Journal of Geophysical Research: Planets*, *126*(5), e2020JE006774. https://doi.org/10.1029/2020JE006774

Sun, M., Gu, H., Cui, J., Wu, X., Huang, X., Ni, Y., Wu, Z., & Li, L. (2023). Enhanced Hydrogen Escape on Mars during the 2018 Global Dust Storm: Impact of Horizontal Wind Field. *The Astrophysical Journal*, *953*(1), 71. https://doi.org/10.3847/1538-4357/ace43e

Vincent, R. A. (1987). Planetary and gravity waves in the mesosphere and lower thermosphere. *Advances in Space Research*, *7*(10), 163–169. https://doi.org/10.1016/0273-1177(87)90089-5

Wang, H., & Richardson, M. I. (2015). The origin, evolution, and trajectory of large dust storms on Mars during Mars years 24–30 (1999–2011). *Icarus*, *251*, 112–127. https://doi.org/10.1016/j.icarus.2013.10.033

Wolff, M. J., Smith, M. D., Clancy, R. T., Arvidson, R., Kahre, M., Seelos, F., Murchie, S., & Savijärvi, H. (2009). Wavelength dependence of dust aerosol single scattering albedo as observed by the Compact Reconnaissance Imaging Spectrometer. *Journal of Geophysical Research: Planets*, *114*(E2), 2009JE003350. https://doi.org/10.1029/2009JE003350

Wolff, M. J., Smith, M. D., Clancy, R. T., Spanovich, N., Whitney, B. A., Lemmon, M. T., Bandfield, J. L., Banfield, D., Ghosh, A., Landis, G., Christensen, P. R., Bell, J. F., & Squyres, S. W. (2006). Constraints on dust aerosols from the Mars Exploration Rovers using MGS overflights and Mini-TES. *Journal of Geophysical Research: Planets*, *111*(E12), 2006JE002786. https://doi.org/10.1029/2006JE002786

Wu, Z., Li, J., Li, T., & Cui, J. (2022). Gravity Waves in Different Atmospheric Layers During Martian Dust Storms. *Journal of Geophysical Research: Planets*, *127*(4), e2021JE007170.

https://doi.org/10.1029/2021JE007170

Wu, Z., Li, T., & Dou, X. (2015). Seasonal variation of Martian middle atmosphere tides observed by the Mars Climate Sounder. *Journal of Geophysical Research: Planets*, *120*(12), 2206–2223. https://doi.org/10.1002/2015JE004922

Wu, Z., Li, T., & Dou, X. (2017). What causes seasonal variation of migrating diurnal tide observed by the Mars Climate Sounder? *Journal of Geophysical Research: Planets*, *122*(6), 1227–1242. https://doi.org/10.1002/2017JE005277

Wu, Z., Li, T., Heavens, N. G., Newman, C. E., Richardson, M. I., Yang, C., Li, J., & Cui, J. (2022). Earth-like thermal and dynamical coupling processes in the Martian climate system. *Earth-Science Reviews*, *229*, 104023. https://doi.org/10.1016/j.earscirev.2022.104023

Wu, Z., Li, T., Li, J., Zhang, X., Yang, C., & Cui, J. (2021). Abnormal Phase Structure of Thermal Tides During Major Dust Storms on Mars: Implications for the Excitation Source of High-altitude Water Ice Clouds. *Journal of Geophysical Research: Planets*, *126*(4), e2020JE006758. https://doi.org/10.1029/2020JE006758

Wu, Z., Li, T., Zhang, X., Li, J., & Cui, J. (2020). Dust tides and rapid meridional motions in the Martian atmosphere during major dust storms. *Nature Communications*, *11*(1), 614. https://doi.org/10.1038/s41467-020-14510-x